Temperature dependence of the structural parameters of gold nanoparticles investigated with EXAFS

T. Comaschi,[1] A. Balerna,[2] and S. Mobilio[1,2]

[1]*Dipartimento di Fisica "E. Amaldi," Università di Roma Tre, via della Vasca Navale 84, I-00146 Roma, Italy*
[2]*Laboratori Nazionali di Frascati INFN, via E. Fermi 40 I-00044 Frascati, Roma, Italy*

The L_3 edge of Au nanoparticles, having sizes ranging from 2.4 to 5.0 nm, have been investigated by x-ray absorption fine structure spectroscopy in the temperature range of 20–300 K. Data were recorded at the European Synchrotron Radiation Facility with a very good signal to noise ratio. To achieve a very high accuracy in the determination of the first shell distance, a very careful data analysis was performed also taking into account the presence of asymmetry effects. In all samples, the temperature dependence of the first neighbor distance results is different from that of the macrocrystalline counterpart. In the largest size samples, a reduction of the thermal expansion was found, whereas in the smallest ones, the presence of a crossover from an initial thermal expansion to a thermal contraction was observed. Calculations based on a simple model show that localization effects that increase as the nanoparticle size decreases can explain the reported thermal effects.

PACS number(s): 78.70.Dm, 71.27.+a, 78.70.Ck

I. INTRODUCTION

Metal nanoparticles show a variety of novel and fascinating electrical, magnetic, and chemical properties arising both from the presence of a large percentage of low coordinated surface atoms and from the confinement of electrons to dimensions shorter than the electron mean free path and the Fermi length.[1,2] From the structural point of view, metallic nanoclusters often undergo a contraction of the lattice distances with respect to bulk materials because of surface stress tension.[3] According to Laplace's law, the lattice parameter is foreseen to linearly decrease with the inverse particle dimension D. Recently, temperature dependent x-ray diffraction measurements on a gold nanoparticle powder (mean dimension of about 4 nm) showed[4] for the first time an additional effect, i.e., the occurrence of a *crossover* in the temperature dependence of the cell parameter, which changes from an initial thermal expansion at low temperatures to a thermal contraction for $T > 125$ K. This result is not due to changes in the structure of the nanoparticle, which continues to show a fcc atomic arrangement as the bulk metal but can be attributed to the contribution of electronic excitations to the total energy of the system. Indeed, for a bulk system, the electronic contribution to the total energy results slowly varies with temperature and, for this reason, bulk materials generally show a thermal expansion, originating from the anharmonicity of the lattice potential.[5] On the other hand,[6,7] in nanoparticles, the presence of electronic discrete energy levels separated by only a few meV implies a relevant variation of the electronic energy with T. In the present paper, we explore more deeply this effect to assess its presence and to quantify it even in smaller clusters, where localization effects are expected to become stronger and stronger. At very low sizes, x-ray diffraction does not allow measuring of the cell parameter of the nanoparticle with sufficient accuracy; therefore, we used x-ray absorption spectroscopy, in particular, the extended x-ray absorption fine structure (EXAFS) region, to get a very accurate estimate of the nearest-neighbor distance as a function of temperature. The experimental behaviors are compared with theoretical

ones estimated assuming a Grüneisen-like model for the thermal expansion modified for the presence of electronic excitations to discrete levels induced by the finite cluster size. The layout of the paper as follows. Section II describes the experimental methods involved for sample preparation and characterization together with the experimental measurements. The results of EXAFS analysis are reported in Secs. III and IV with a first outlook at low temperature results in the first section and at the temperature behavior in the second one. Sections V and VI are dedicated to the discussion of the results and to the conclusions. The Appendix reports the main details of the EXAFS data handling used to extract the corresponding structural parameters.

II. SAMPLE PREPARATION AND CHARACTERIZATION: X-RAY ABSORPTION MEASUREMENTS

The characteristics of the five gold nanoparticle samples investigated are reported in Table I. Au-NP1 and Au-NP2, supported on amorphous silica, were prepared from high purity Au foil as described in Refs. 8 and 9 using the solvated metal atom dispersion (SMAD) technique. This method involves the following steps: (a) deposition of an organic solvent (acetone or a mixture of acetone and thiol for the production of thiol-capped nanoparticles) on the reactor walls cooled at 77 K, (b) vaporization of the metal under vacuum

TABLE I. List of the investigated samples with the corresponding main characteristics.

Sample	Preparation	$\bar{D}$ (Å)	$\sigma_{\bar{D}}$ (Å)	Type	Support
Au-NP1	SMAD	50 ± 7		Not coated	SiO_2
Au-NP2	SMAD	40 ± 6		Not coated	SiO_2
Au-NP3	Evaporation	42 ± 8	5	Not coated	Mylar
Au-NP4	Evaporation	24 ± 8	8	Not coated	Mylar
Au-SR1	SMAD	28 ± 5		Thiol capped (dodecanethiol)	SiO_2

and then rapid trapping of the metal atoms by the frozen solvent matrix, and (c) warming up to room temperature of the solvated gold atoms. The solvated metal atom solution was used to impregnate a weighted amount of high surface area amorphous silica. After impregnation, the samples were degassed and dried at room temperature under vacuum. Au-NP3 and Au-NP4 samples were produced under vacuum on a 6 μm polymer film by consecutive evaporation of gold and Mylar to achieve the optimum metal thickness for the x-ray measurements. The Mylar thickness between different gold layers was always around 200 Å. Film thicknesses were controlled with a quartz-crystal detector. Au-SR1 is a thiol-capped nanoparticle prepared according to the SMAD technique and capped with dodecanethiol molecules [$CH_3(CH_2)_{10}CH_2SH$].

All samples were characterized by x-ray powder diffraction performed at the GILDA beamline BM8 of the European Synchrotron Radiation Facility (ESRF) of Grenoble.[10] Measurements were carried out at fixed wavelength (0.688 67 Å) and at room temperature using an imaging plate as detector (Fuji, 200×400 mm^2). The experimental data were analyzed according to the Scherrer analysis[11] of the diffraction peaks to obtain the cluster mean size of each sample; the instrumental resolution was determined using a standard. The values obtained are reported in Table I.

Samples Au-NP3 and Au-NP4 were characterized also with transmission electron microscopy, which provided the size dispersion σ_D reported in the table. The size dispersion of samples Au-NP1 and Au-NP2 was not measured but the specific growth conditions used to prepare SMAD samples Au-NP1 and Au-NP2 ensure the achievement of a narrow size distribution,[12] surely sharper than that of samples prepared by evaporation, Au-NP3 and Au-NP4. The experimental uncertainty reported for $\bar{D}$ values in Table I was estimated by applying the propagation error formula to the Scherrer relation and must be considered an upper limit of the uncertainty in the $\bar{D}$ values.

X-ray absorption (XAS) measurements were performed at the BM08 (GILDA) beamline of ESRF in Grenoble (France). The electron energy and average current were 6 GeV and 190 mA, respectively. The spectra were recorded at the L_3 edge of Au in transmission mode. The x-ray beam was monochromatized by two silicon (311) crystals, detuned to reduce the higher harmonics contribution. The beam intensity was measured before and after the sample by two argon filled ionization chambers. The sample temperature was varied from 20 up to 300 K using a liquid helium cryostat, with the sample immersed in He gas atmosphere. The integration time was 4 or 5 s per point depending on the energy interval. In some cases, to increase the signal to noise ratio, two or three spectra were measured and then averaged.

EXAFS spectra $\chi(k)$ were extracted from the experimental x-ray absorption coefficient according to standard procedures, as described in the Appendix. The $\chi(k)$ is given by

$$\chi(k) = S_0^2 \sum_j \frac{N_j}{kR_j^2} A(k,R_j) e^{-2\sigma_j^2 k^2} e^{-2(R_j/\lambda)} \sin(kR_j + \phi(k,R)), \quad (1)$$

where the sum is over the different coordination shells around the absorbing atom. S_0^2 is the amplitude scaling factor

TABLE II. Structural parameters at 20 K for Au-NP1, Au-NP2, Au-NP3, and Au-NP4 at 20 K obtained using the ratio method and Au bulk as reference.

	Samples at 20 K		
Sample	N	R (Å)	σ^2 (10^{-2} Å^2)
Bulk	12.0	2.876(2)	0.17(1)
Au-NP1	11.8(5)	2.872(2)	0.23(1)
Au-NP2	10.5(5)	2.869(2)	0.32(2)
Au-NP3	11.0(5)	2.867(2)	0.29(2)
Au-NP4	9.1(3)	2.847(2)	0.40(2)

reflecting the contribution of multielectron processes; $A(k,R)$ and $\phi(k,R)$ represent the effective backscattering amplitude and total phase; R is the distance of neighboring atoms from the central absorber; N is the corresponding coordination number, while σ^2 is the variance associated with the distribution of the distance R (mean square relative displacement). The first coordination shells were analyzed in two different ways using a phenomenological approach (ratio method)[13] and a theoretical procedure (best fit).[14] In order to take into account asymmetry effects, whose importance increases with increasing temperature and with decreasing size, the cumulant expansion method was used, and in the Appendix, this very accurate data analysis method for the first coordination shell is described in detail. The two data analysis procedures used gave the same results within the experimental errors; the overall accuracy in the first neighbor distance was about 2×10^{-3} Å. This was also true for the Au-SR1 sample, where the Au-S and Au-Au contributions can be separated well; the former contribution was analyzed only by the fitting procedure using the phase provided by FEFF, the latter with both procedures as for all the other samples. Higher order coordination shells were analyzed through a best-fit procedure of the experimental EXAFS signal, which also takes into account multiple scattering effects.

III. EXTENDED X-RAY ABSORPTION FINE STRUCTURE RESULTS AT 20 K

The values of N, R, and σ^2 for the first coordination shell of the five nanoparticle samples at 20 K are reported in Table II for the not-coated samples and in Table III for Au-SR1; for the latter, a coordination shell due to sulfur atoms is present, originated by the dodecanethiol capping molecule.

A contraction of the interatomic distances, a reduction of the coordination numbers, and an increase of the structural disorder with decreasing size are evident from the results, in agreement with previous studies.[3,15,16]

Indeed, lattice contraction is expected to occur in metallic finite-size systems due to surface stress according to the Laplace law:

$$\Delta R = -\frac{4}{3} K_B R_B f \frac{1}{D}, \quad (2)$$

where K_B is the bulk compressibility, R_B the bulk nearest-neighbor distance (NND), f the surface stress, and D the

TABLE III. Structural parameters associated with the first two coordination shells (Au-S and Au-Au) for Au-SR1 at 20 K obtained through a best fit of the corresponding EXAFS signal.

			Au-SR1 at 20 K			
N_S	R_S (Å)	σ_S^2 $(10^{-2}$ Å$^2)$	N_{Au}	R_{Au} (Å)	σ_{Au}^2 $(10^{-2}$ Å$^2)$	
2.2(4)	2.286(2)	0.65(5)	8.2(4)	2.861(2)	0.31(5)	

mean cluster diameter. ΔR values of Au-NPi samples are in agreement with those reported in Refs. 15 and 16 and show a linear behavior of ΔR with respect to D^{-1} according to Eq. (2).[17] From the slope of this linear trend, we got a value of $f = 3.8 \pm 0.3$ J/m^2, in good agreement with the values previously determined.[15,16,18] As expected, the value of f found for the clusters is about 1.4 times larger than the f value of gold bulk ($f = 2.7$ J/m^2).[19]

The tabulated values of N are in good agreement with those expected from the size of the clusters assuming a spherical shape of the nanoparticle. The decrease of N is due to the reduced mean coordination of the atoms inside the clusters, a consequence of the higher and higher percentage of surface atoms lacking neighbors as the nanoparticle size decreases. Correspondingly, an enhanced structural disorder is also expected because of higher asymmetry effects connected to the finite dimension of the systems and of a higher mobility of the surface atoms.

To confirm the fcc crystallographic structure of the clusters as suggested by XRD, the whole experimental EXAFS signals of the five samples at 20 K were fitted with simulated spectra built up assuming a fcc structure. The best-fit procedure was based on the CERN-LIB MINUIT package. The simulated spectra included both single scattering and multiple scattering contributions originating from the first four coordination shells. Amplitudes and phases for the different paths were calculated by the FEFF8 code assuming a fcc atomic arrangement. For all measurements done at 20 K, we assumed that anharmonic effects were negligible and so a Gaussian distance distribution was used for all shells in the fitting procedure. E_0 parameter was fixed at a mean value equal to 7.3 eV above the nominal E_0 value of the bulk (11 919 eV); S_0^2 parameter was maintained at the fixed value of 0.9 taken from the best fit of the gold bulk datum. The best fits in k space and in r space are shown in Figs. 1 and 2.

The very good quality of the fits confirms the presence of a fcc structure in all the samples; therefore, it is possible to conclude that the atomic arrangement is prevalently the same as the bulk material one even for the smallest nanoparticles investigated.

The values of coordination numbers, distances, and Debye-Waller factors obtained for the four shells are reported in Table IV. The σ^2 values for the fourth coordination shell are not reported because this shell includes also multiple scattering contributions; the rather high correlation between the σ^2 values due to single scattering and to multiple scattering paths prevented us from obtaining reliable quantitative values.

IV. EXTENDED X-RAY ABSORPTION FINE STRUCTURE RESULTS AS A FUNCTION OF T

As for the temperature dependence of the structural parameters of the first coordination shells, an accurate data treatment was performed, as described in the Appendix. The cumulant method was used to take into account anharmonic effects which become more and more important as the temperature increases. From the analysis, the cumulants of the nearest-neighbor distance distribution, usually indicated as C_1^*, C_2^*, C_3^*, which are, respectively, the mean interatomic distance, the Debye-Waller factor, and the asymmetry in the distance distribution, can be achieved.

In the analysis of the spectra at each T, the coordination numbers were assumed to be equal to the values in Tables II and III obtained at 20 K.

In Fig. 3, we report the thermal behavior of the EXAFS Debye-Waller factors ΔC_2^*, usually referred to as $\Delta\sigma^2$. According to Ref. 20 such behaviors are approximated well by a Debye correlated model, as clearly shown in the figure. The values of the corresponding Debye temperatures are reported in Fig. 3; all values are less than the bulk one ($\theta_B = 170$ K), in agreement with previous studies. Such a decrease of the Debye temperature is due to the higher mean mobility of the atoms of the cluster with respect to the bulk ones.[16]

In addition, comparing the θ_D values of samples prepared by the same method (i.e., Au-NP1 with Au-NP2 and Au-NP3 with Au-NP4), we observe a decrease of the Debye temperature with decreasing size, in agreement with the increased percentage of surface atoms as the size decreases.

In Fig. 4, we report the thermal behavior of the mean interatomic distance ΔC_1^*, usually indicated as ΔR; such values were obtained from the accurate data analysis described in the Appendix and are relative to the values achieved at 20 K.

Quite marked differences between the different samples are evident. Au-NP1, the one with the greatest nanoparticle size, has a bulklike trend with slightly lower ΔR values. On the contrary, Au-NP2 at low T has a bulklike behavior, while over 170 K, its ΔR values do not grow as in the bulk case and become much lower than the bulk ones as the temperature increases up to 300 K. Au-NP3, the greatest sample of the two produced using evaporation, shows a thermal behavior similar to Au-NP1. As Au-NP2, Au-NP4 also follows the bulk behavior at low temperatures, while over 200 K, the achieved ΔR values are quite lower than the bulk ones. Finally, the Au-SR1 sample shows a nearly zero expansion in the investigated temperature range. The thermal behaviors observed for Au-NP1 and Au-NP3 and for Au-NP2 and Au-
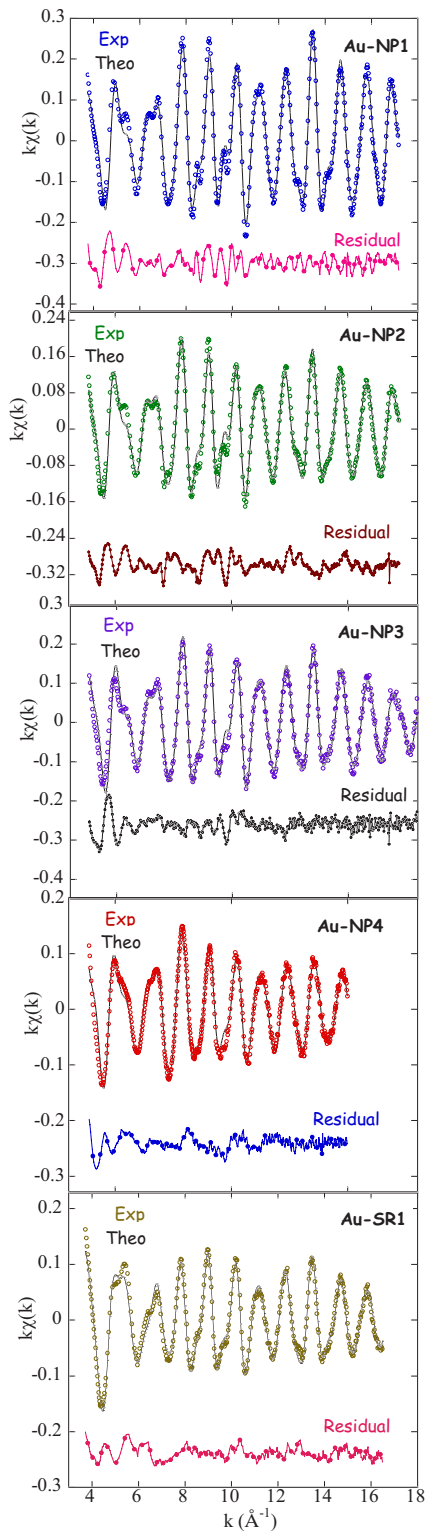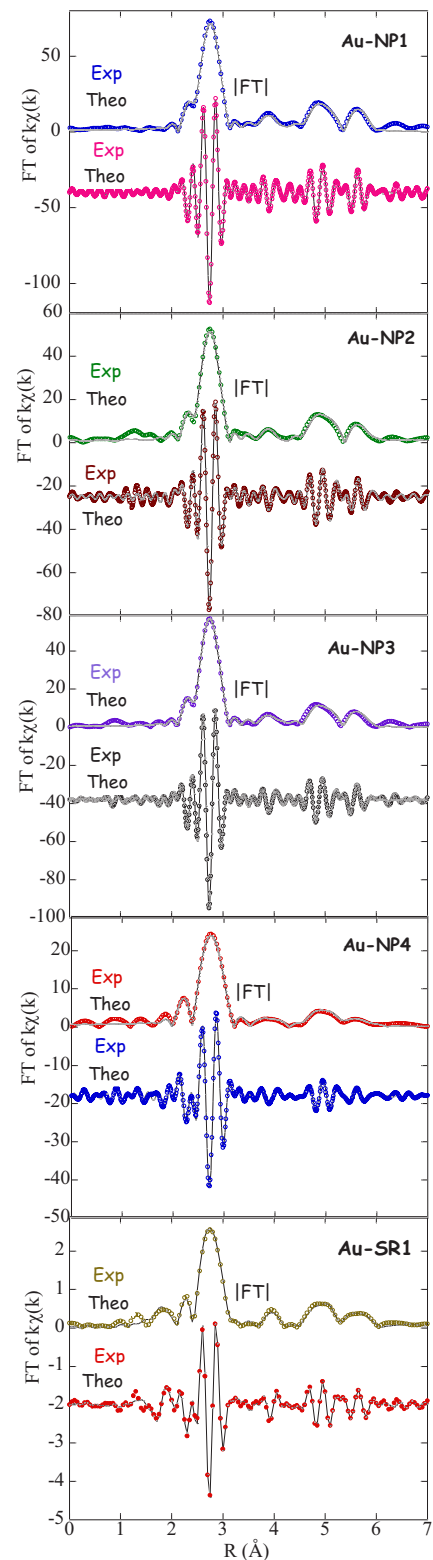
FIG. 1. (Color online) Best fit in *k* space of the experimental EXAFS signals at 20 K for the different samples. The continuous line is the best-fit curve superimposed on the experimental points.

FIG. 2. (Color online) Best fit in *r* space of the experimental EXAFS signals at 20 K for the different samples. The continuous line is the best-fit curve superimposed on the experimental points.

NP4 are very similar also if the samples of both couples were grown on different substrates (SiO_2 and Mylar). The thermal expansion coefficient of SiO_2 (4×10^{-6} K^{-1}) is about four times lower than the Au bulk one (1.4×10^{-5} K^{-1}), while that of Mylar (5×10^{-5} K^{-1}) is about four times higher. Such a

big difference between Mylar and SiO_2 does not seem to have a significant influence on the nanoparticle thermal behavior.

TABLE IV. Structural parameters (coordination number, distance, and Debye-Waller factor) at 20 K for higher order coordination shells of gold atoms for all samples.

	No. of shell	N	R (Å)	σ^2 (10^{-2} Å^2)
Au-NP1	2	5.9(5)	4.061(8)	0.31(8)
	3	23.6(5)	4.975(6)	0.33(8)
	4	11.8(5)	5.745(6)	
Au-NP2	2	5.3(5)	4.057(8)	0.49(8)
	3	21.0(5)	4.969(6)	0.43(8)
	4	10.5(5)	5.737(6)	
Au-NP3	2	5.5(5)	4.055(8)	0.52(8)
	3	22.0(5)	4.965(6)	0.55(8)
	4	11.0(5)	5.734(6)	
Au-NP4	2	4.5(5)	4.026(8)	0.80(8)
	3	18.2(5)	4.931(6)	0.76(8)
	4	9.1(5)	5.694(6)	
Au-SR1	2	4.1(5)	4.061(8)	0.37(8)
	3	16.4(5)	4.974(6)	0.50(8)
	4	8.2(5)	5.743(6)	

V. DISCUSSION

In agreement with the XRD results,[4] we observed the occurrence of clearly reduced thermal expansion effects in the investigated samples; this effect depends on the size of the cluster and on the preparation method.

In Ref. [4], the presence of a negative thermal expansion in gold clusters was interpreted as due to the presence of discrete electronic energy levels induced by the finite size of the nanoparticle. In order to have an understanding of the thermal behavior of our samples, we have calculated the thermal behavior of the nearest-neighbor distance for approximately spherical gold nanoclusters of different sizes. We considered the total energy of the system as a sum of three main contributions:

$$E_{tot} = U + E_{vib} + E_{el}, \tag{3}$$

where U, E_{vib}, and E_{el} are the static, the vibrational, and the electronic energy of the nanoparticle, respectively. The temperature-independent part of the total energy is represented by the static term U, which was expressed as

$$U = -\frac{A}{r^m} + \frac{B}{r^n}, \tag{4}$$

where A and B are numerical constants connected to the compressibility and the equilibrium volume of the system, m and n are numerical constants depending on gold, while r represents the interatomic distance.

E_{vib} was calculated as the energy of a finite series of harmonic oscillators, which, in the Debye approximation, is given by

$$E_{vib} = \frac{3}{2\pi^2} \frac{(k_B T)^4}{(\hbar v)^3} V \int_0^{x_D} \frac{x^3}{e^x - 1} dx, \tag{5}$$

where V is the equilibrium volume of the system, v is the velocity of sound, and x_D is the Debye fraction, $x_D = \frac{\hbar \omega_D}{k_B T}$. Anharmonic effects were introduced into Eq. (5) by considering the volume dependence of the phonon frequencies, described by the Grüneisen parameter, γ:

$$\gamma = -\frac{d \ln \omega}{d \ln V}. \tag{6}$$

From this relation, we get a volume dependence of ω as $\omega = CV^{-\gamma}$, where C is a numerical constant. The Debye approximation foresees a linear dispersion relation for sound waves propagating in an isotropic medium: $\omega = v_0 k$, where v_0 is the velocity of sound at temperature T_0 and V_0 is the volume at the same temperature. From these two equations at T_0, where $\omega = CV_0^{-\gamma} = v_0 k$, we obtain the following for C:

$$C = \frac{v_0 k}{V_0^{-\gamma}}. \tag{7}$$

At all temperatures T, when the volume is V, we obtain the following for ω:

$$\omega = CV^{-\gamma} = v_0 \left(\frac{V}{V_0}\right)^{-\gamma} k. \tag{8}$$

Assuming a spherical shape for the nanocluster with diameter D (D_0), the Debye frequency and the vibrational energy, respectively, become

$$\omega_D = v_0 (36\pi N)^{1/3} \frac{D^{-3\gamma - 1}}{D_0^{-3\gamma}} \tag{9}$$

and

$$E_{vib} = \frac{1}{4\pi} \frac{(k_B T)^4}{(\hbar v_0)^3} \frac{D^{3+9\gamma}}{D_0^{9\gamma}} \int_0^{x_D} \frac{x^3}{e^x - 1} dx. \tag{10}$$

In the calculations for the velocity of sound, we also used the bulk value $v_0 = 1740$ m/s for the clusters; this is justified by the rather small variations of the Debye temperature of the clusters with respect to the bulk value (a few percent), as reported in Fig. [3].

The electronic contribution to the total energy was treated according to Kubo.[7] In this approach, the discrete energy level distribution, E_n, induced by the finite particle size, which also depends on the particle shape and surface conditions, is averaged and assumed to be an equally spaced energy level distribution with a mean spacing given by

$$E_n(D) = n\Delta(D) \propto n\frac{1}{D^3}, \tag{11}$$

where D is the particle's diameter. The electronic contribution was approximated as a sum of discrete energy levels, E_n, each one weighted with its own occupation number, $f(E_n)$:

$$E_{el} = -N_e \sum_n E_n(D)f(E_n), \qquad (12)$$

where N_e is the number of valence electrons.

The total energy of the different nanoparticles was calculated as a function of their diameter at each temperature (Fig. 5). The minimum of the total energy at each T represents the equilibrium size of the system at that T. In this way, we obtained the theoretical trends of the NND as a function of T for some nominal sizes. The variation of NND with respect to the value at 20 K is reported in Fig. 6. The different thermal behaviors are originated by the different balances between the vibrational energy (leading to positive expansion with increasing T) and the electronic energy (leading to negative thermal expansion), which changes as a function of the nanoparticle size.

In Fig. 6, the excellent agreement between the so calculated thermal expansions of the bulk with the values experimentally observed is clearly visible, which confirms that anharmonic effects are properly taken into account by our model. We observe from Fig. 6 that our calculations foresee three regimes:

(a) for high cluster dimensions, a bulklike behavior with a reduced thermal expansion;

(b) for intermediate cluster sizes, a crossover from a reduced thermal expansion at low T to a negative thermal expansion at high T with a crossing temperature which lowers at smaller dimensions; and

(c) a nearly zero thermal expansion for low sizes.

We underline that such behaviors are in qualitative agreement with the observed ones, reported in Fig. 4 and described above. In particular, by comparing the behavior of NP1 with that of NP2 and the behavior of NP3 with that of NP4, we observe how a decrease of the cluster size in samples prepared with the same technique (SMAD and evaporation, respectively) induces the crossover from (a)-like to (b)-like behavior. On the other hand, the Au-SR1 sample, the sample with the smallest size, shows a nearly zero thermal behavior, in agreement with the behavior foreseen by the model for low size clusters.

The behaviors of samples NP2 and NP3 seem to be contradictory because the two samples have the same nominal mean size while showing different thermal behaviors. We remind here that these two samples were prepared according to different methods (SMAD and evaporation, respectively) and this is reflected in the rather sharper size distribution of NP2 with respect to NP3. Taking into account that x-ray absorption makes a volume-weighted average of the particles, it comes out that a wide size distribution gives rise to an overall behavior that reproduces that of the nanoparticles with diameters larger than the average nominal value. For this reason, the NP3 sample whose average D value is 4.2 nm shows a thermal behavior more similar to that of the NP1 sample whose average dimension is 5 nm than to that of NP2. For the same reason the first shell coordination number of sample NP3 is higher than that of sample NP2 (Table II).

VI. CONCLUSIONS

In this work, an EXAFS study of five samples of gold nanoparticles in the temperature range from 20 to 300 K has
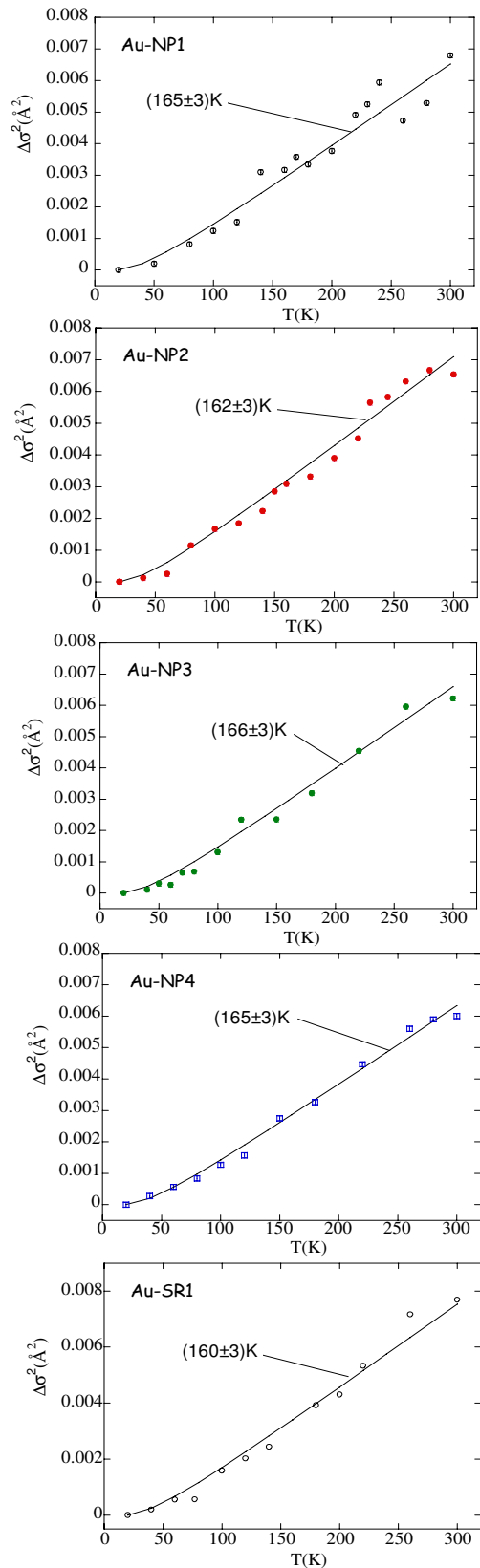

FIG. 3. (Color online) Relative variations of the Debye-Waller factors as a function of temperature for the first coordination shell of the different investigated samples. The superimposed lines correspond to the theoretical curves calculated according to a Debye correlated model, fitted to the experimental points.
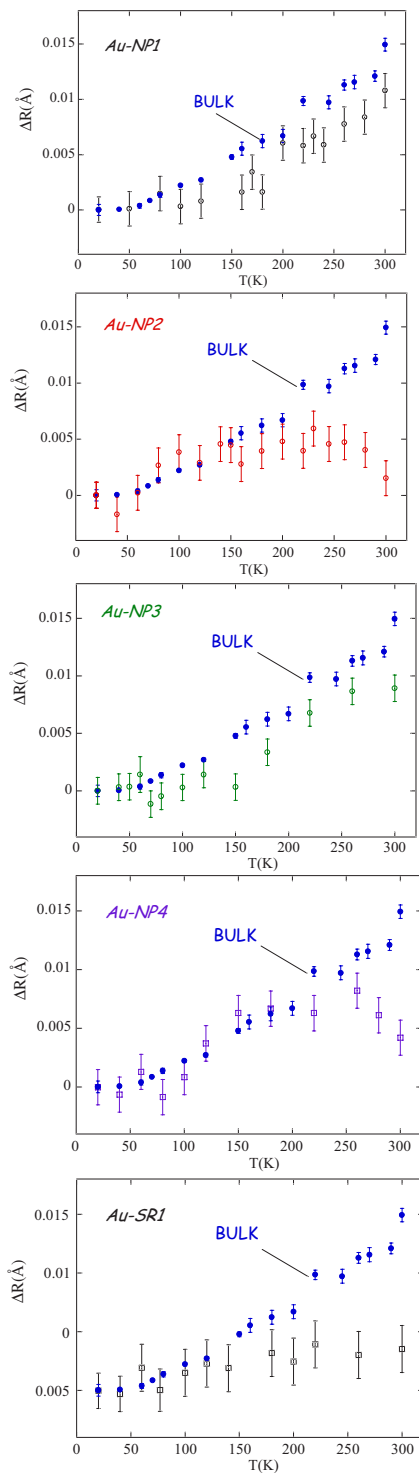
FIG. 4. (Color online) Relative variations as a function of T of the near-neighbor distance for the five investigated samples compared to the corresponding thermal trend for gold bulk (depicted with blue circles). ΔR indicates the R values relative to the 20 K ones.

been presented. Our results exclude the presence of a structural phase transition at any T for each cluster dimension. The nanoparticles all show a fcc structure. An accurate analysis was performed for the first coordination shell in order to see how the thermal behavior of such confined objects
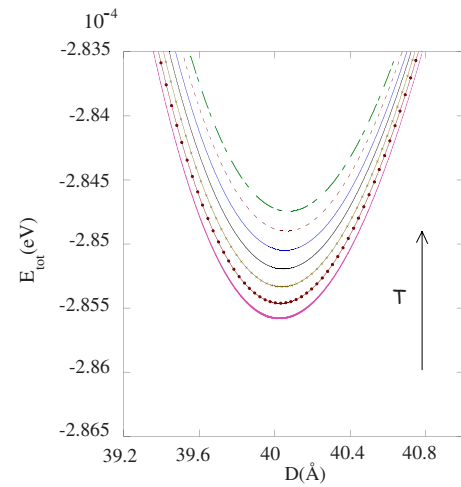
FIG. 5. (Color online) Curves of the total energy of the system near the minimum for a mean diameter of the nanoparticle equal to 40 Å at different temperatures.

changes with decreasing their size. To properly take into account asymmetry effects, the cumulant expansion method was adopted for the first shell data analysis.

For all the nanoparticles the temperature dependence of the first shell interatomic distances found was different from that of the macrocrystalline counterpart. In the largest samples, a reduction of the variations of the interatomic distances with respect to the bulk was observed, which, in the smaller systems, do not increase anymore with T. The thiol-capped nanoparticles show a constant behavior of the first coordination shell distance with increasing T. These behav-
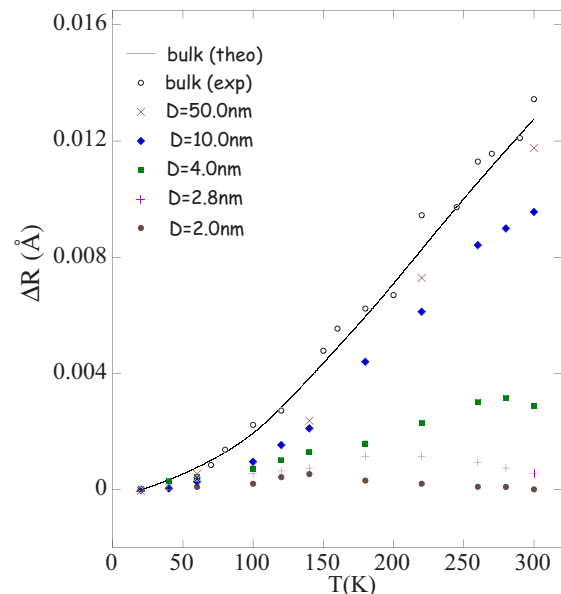

FIG. 6. (Color online) Comparison between the experimental thermal expansion of gold bulk and thermal expansion predicted from our calculations for a bulklike system together with the theoretical trends with T of the relative values of the mean interatomic distance for different nominal sizes of the nanocluster. For the constants γ, m, and n, we used the values characteristic of Au bulk equal to 2.36, 5.2, and 12.2, respectively, from Ref. 22.
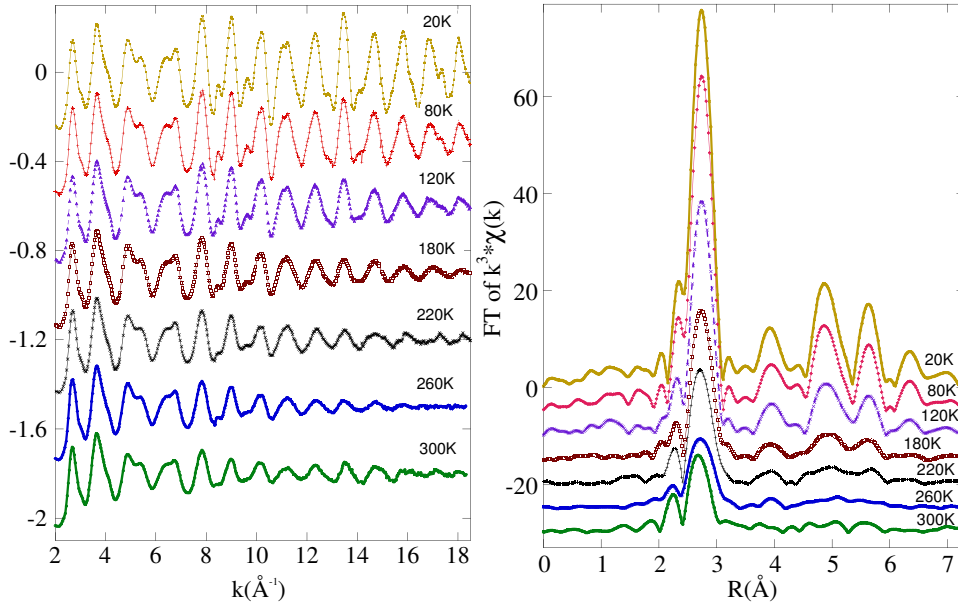
FIG. 7. (Color online) EXAFS function (on the left) and corresponding Fourier transforms (on the right) at different temperatures for Au-NP1.

iors are in quite good agreement with calculations based on the energy contribution of the electronic energy levels induced by the finite nanoparticle size.

The results presented in this paper contribute to a deeper understanding of the localization effects on the structural properties of noble metal nanoparticles.

APPENDIX: DATA TREATMENT AND FIRST SHELL DATA ANALYSIS

First of all, the Au L_3 absorption edges of all spectra were aligned to within about 0.1 eV comparing with the experimental spectra in the x-ray absorption near-edge structure region as a function of $E - E_0$. Then, the spectra were analyzed according to a standard procedure to extract the oscillating part of the spectrum, $\chi(k)$, defined as

$$\chi(k) = \frac{\mu_{L_3}(k) - \mu_0(k)}{\mu_0(k)}, \tag{A1}$$

where $\mu_{L_3}(k)$ is the Au L_3-shell contribution to the absorption coefficient, $\mu_0(k)$ is the atomic absorption coefficient about which $\mu_{L_3}(k)$ oscillates, and k is the photoelectron wave vector given by

$$k = \left[\frac{2m(E - E_0)}{\hbar^2}\right]^{1/2}, \tag{A2}$$

where E is the incoming photon energy and E_0 is the threshold energy. μ_0 was calculated using three or more polyno-

mial curves to approximate the smooth variations of the atomic absorption coefficient while E_0 was determined as the inflection point of the measured absorption edge.

The EXAFS oscillations so obtained at selected temperatures are shown in Fig. 7 for Au-NP1. Figure 7 also shows the corresponding Fourier transforms (FTs). The first peak at about 2.3 Å corresponding to the first coordination shell is isolated well at all temperatures. For this reason, it can be Fourier backtransformed to get the first shell contribution to the EXAFS signal as well as its phase $\phi(k,R)$ and amplitude $A(k,R)$. The other peaks in the FTs correspond to higher order coordination shells and are due to single scattering contributions as well as to multiple scattering effects. In order to obtain accurate quantitative information on the first coordination shell we adopted a phenomenological approach known as the ratio method and a theoretical approach based on a nonlinear best fit of the experimental signal of the first coordination sphere.[14,21] Both methods gave the same results within the experimental error bars.

In harmonic approximation, the general form of the fine structure of the absorption coefficient $\chi(k)$ is given by Eq. (1).

It is well known that such harmonic approximation cannot be used when a high accuracy in the distance determination is required for the presence of effects due to the anharmonicity of the interatomic potentials, which reflects into non-Gaussian and asymmetric distribution functions. Such effects can be taken into account using the cumulant expansion method.[13]

In this approximation, the $\chi(k)$ is given by

$$\chi(k) = S_0^2 \frac{N}{kR^2} A(k,R) e^{-2C_2 k^2} e^{-2(R/\lambda)} \sin\left(2kC_1 + \phi(k,R)\right.$$
$$\left. - \frac{4}{3}C_3 k^3 + \cdots\right), \tag{A3}$$

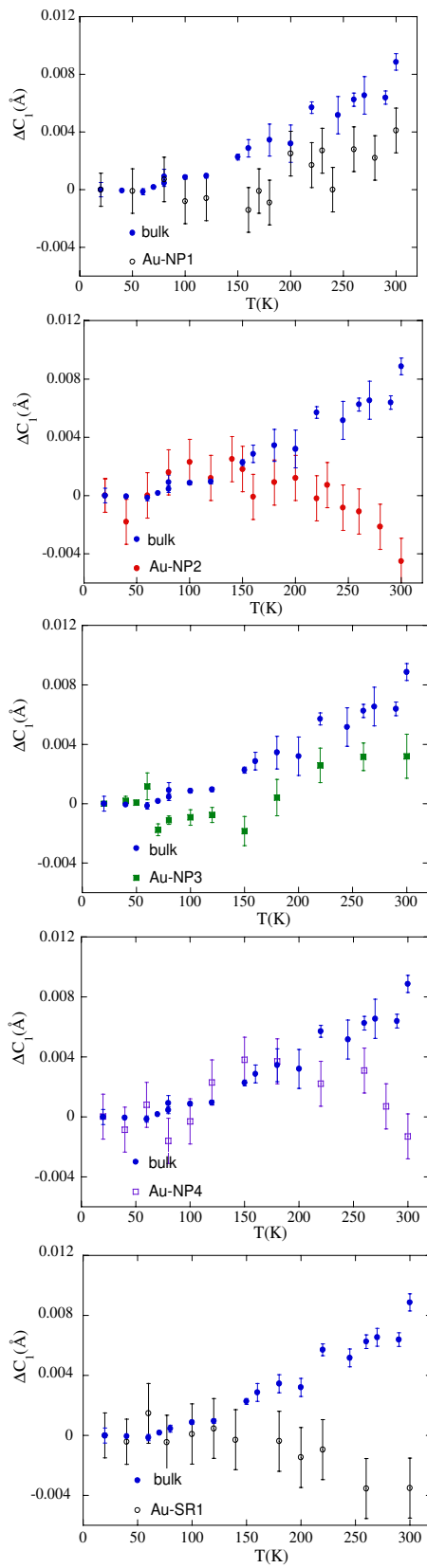where C_1, C_2, and C_3 are the cumulants of the effective

FIG. 8. (Color online) Relative variations as a function of T of the first cumulant of the effective distribution for the first shell of the four investigated samples compared to the corresponding thermal trend for gold bulk (depicted with blue circles).
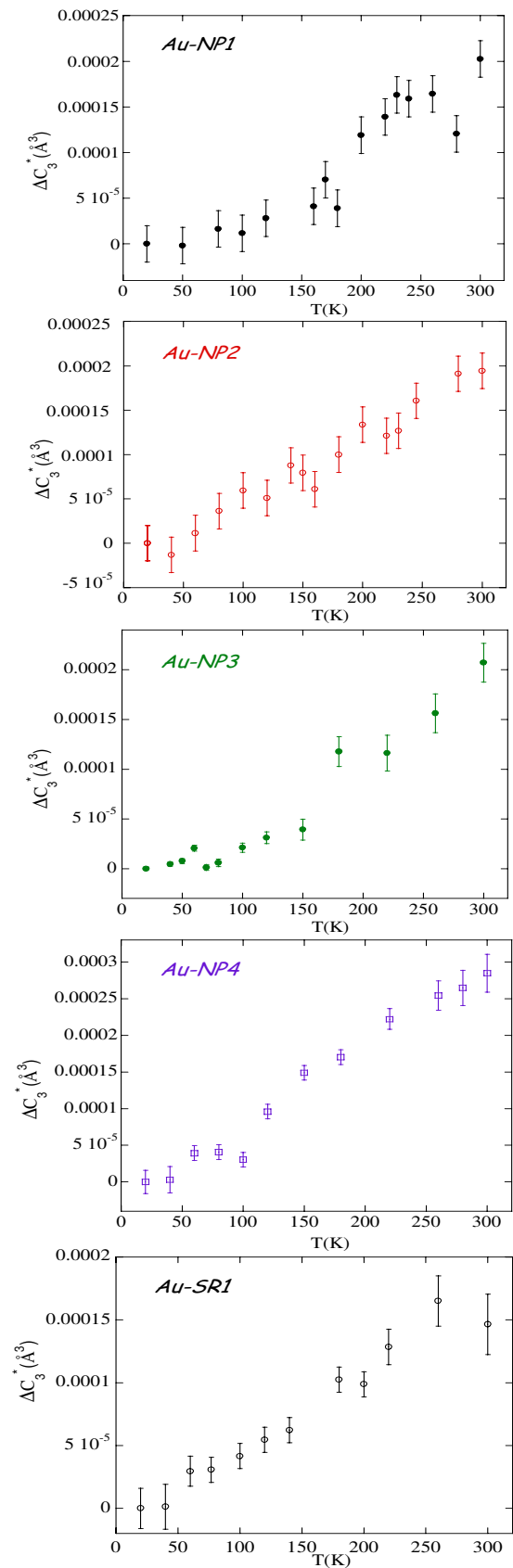
FIG. 9. (Color online) Relative variations as a function of T of the third cumulant for the first shell of the four investigated samples.

distance distribution of nearest-neighbor atoms around the absorber.

C_1 is the mean interatomic distance value, C_2 is the variance, and C_3 is the asymmetry of the corresponding distance distribution. We have omitted higher order cumulants because they resulted to be unessential.

Starting from Eq. (A3) and using the ratio method, phase $\phi(k,R)$ and amplitude $A(k,R)$ functions of the first shell EXAFS signals obtained by the back-Fourier transforms were compared according to the following equations:

$$\frac{\phi_s(k,R) - \phi_r(k,R)}{2k} = \Delta C_1 - \frac{2}{3}k^2\Delta C_3 + \cdots, \qquad (A4)$$

$$\ln\left[\frac{A_s(k,R)}{A_r(k,R)}\right] = \ln\frac{N_s(k)}{N_r(k)} - 2k^2\Delta C_2 + \cdots, \qquad (A5)$$

where the subscripts s and r indicate the sample and the reference compound, respectively. From this type of analysis, we got the values of the structural parameters, ΔC_i, relative to the reference spectrum.

From the relative values of $\Delta C_i = C_i^{sample} - C_i^{reference}$, we have got the absolute values C_i^{sample} simply by summing the C_i values of the reference obtained from the analysis of the bulk spectrum at 20 K performed in the hypothesis of a Gaussian distribution.

In Fig. 8, we show the relative values, ΔC_1, obtained as a function of temperature for the different samples, together with that of the gold bulk. Relevant differences between the two behaviors can be observed.

We remind here that the values of the cumulants C_i are not the cumulants of the real pair distribution function but of an effective pair distribution function, as explained in Ref. 23. To get the C_i^* values of the real pair distribution function, the so obtained values of the cumulants C_i have to be transformed into C_i^*. According to Refs. 23 and 24, such a correction is significant only for the first cumulant and is given by

$$C_1 = C_1^* - \frac{2C_2^*}{C_1^*}\left(1 + \frac{C_1^*}{\lambda}\right). \qquad (A6)$$

For the mean free path λ, we used a value of 9 Å, which is a reasonable value for gold bulk. The values of the first two cumulants so obtained are usually indicated as ΔR and $\Delta\sigma^2$, respectively, and are those reported in Figs. 4 and 3.

The results obtained through the ratio method were compared with those extracted from the simulation and best fit of the EXAFS spectra at different temperatures performed with the FEFF8 code. In this case, in order to reduce the number of free parameters in the fit, we fixed E_0 to an average value equal for all spectra[24] and S_0^2 to the value found for the bulk spectra. Good agreement was found between the two methods at each temperature.

For completeness, we report in Fig. 9 the thermal behaviors of ΔC_3^*; in all samples, such third cumulant increases with temperature, as expected, and its variations are quite similar to the bulk ones.[25]

[1] W. De Heer, Rev. Mod. Phys. **65**, 611 (1993).

[2] W. P. Halpherin, Rev. Mod. Phys. **58**, 533 (1986).

[3] A. Balerna, E. Bernieri, P. Picozzi, A. Reale, S. Santucci, E. Burattini, and S. Mobilio, Phys. Rev. B **31**, 5058 (1985).

[4] W.-H. Li, S. Y. Wu, C. C. Yang, S. K. Lai, K. C. Lee, H. L. Hunag, and H. D. Yang, Phys. Rev. Lett. **89**, 135504 (2002).

[5] N. W. Ashcroft and N. D. Mermin, *Solid State Physics* (Holt-Sauders International Edition, Tokyo, 1981).

[6] D. Davidovic and M. Tinkham, Phys. Rev. Lett. **83**, 1644 (1999).

[7] R. Kubo, J. Phys. Soc. Jpn. **17**, 975 (1962).

[8] K. J. Klabunde, Y. X. Li, and B. J. Tan, Chem. Mater. **3**, 30 (1991).

[9] M. P. Casaletto, A. Longo, A. M. Venezia, and A. Martorana, and A. Prestianni, Appl. Catal., A **302**, 309 (2006).

[10] S. Pascarelli, F. Boscherini, F. D'Acapito, J. Hrdy, C. Meneghini, and S. Mobilio, J. Synchrotron Radiat. **3**, 147 (1996).

[11] B. E. Warren, *X-ray Diffraction* (Addison-Wesley, Reading, MA, 1990).

[12] K. J. Klabunde, *Free Atoms, Clusters and Nanoscale Particles* (Academic, New York, 1994); A. Longo (private communication).

[13] G. Bunker, Nucl. Instrum. Methods Phys. Res. **207**, 437 (1983); P. Fornasini, J. Phys.: Condens. Matter **13**, 7859 (2001).

[14] A. L. Ankudinov, B. Ravel, J. J. Rehr, and S. D. Conradson, Phys. Rev. B **58**, 7565 (1998); M. Newville, B. Ravel, J. Rehr, E. Stern, and Y. Yacoby, Physica B **208-209**, 154 (1995).

[15] P. Kluth, B. Johannessen, G. J. Foran, D. J. Cookson, S. M. Kluth, and M. C. Ridgway, Phys. Rev. B **74**, 014202 (2006).

[16] A. Balerna and S. Mobilio, Phys. Rev. B **34**, 2293 (1986).

[17] C. W. Mays, J. S. Vermaak, and D. Kuhlmann-Wilsorf, Surf. Sci. **12**, 134 (1968).

[18] A. Balerna, E. Bernieri, P. Picozzi, A. Reale, S. Santucci, E. Burattini, and S. Mobilio, Surf. Sci. **156**, 206 (1985).

[19] R. J. Needs and M. Mansfield, J. Phys.: Condens. Matter **1**, 7555 (1989).

[20] G. Beni and P. M. Platzman, Phys. Rev. B **14**, 1514 (1976).

[21] P. A. Lee, P. H. Citrin, P. Eisenberger, and B. M. Kincaid, Rev. Mod. Phys. **53**, 769 (1981).

[22] F. C. Nix and D. MacNair, Phys. Rev. **60**, 597 (1941); M. Born and K. Huang, *Dynamical Theory of Crystal Lattices* (Oxford University Press, New York, 1954); N. W. Ashcroft and N. D. Mermin, *Solid State Physics* (Holt-Sauders International Edition, Tokyo, 1981); S. Topaldi, J. Phys. F: Met. Phys. **4**, 2138 (1974).

[23] P. Fornasini, F. Monti, and A. Sanson, J. Synchrotron Radiat. **8**, 1214 (2001).

[24] P. Fornasini, S. a Beccara, G. Dalba, R. Grisenti, A. Sanson, M. Vaccari, and F. Rocca, Phys. Rev. B **70**, 174301 (2004).

[25] T. Comaschi, A. Balerna, and S. Mobilio (unpublished).